Hard X-ray Photon-in Photon-out Spectroscopy as a Probe of the Temperature-Induced Delocalization of Electrons in Nanoscale Semiconductors

Hirsch, O.; Kvashnina, K.; Willa, C.; Koziej, D.;

Perma-Link to Publication Repository of HZDR:

https://www.hzdr.de/publications/Publ-24257

Hard X-ray photon-in photon-out spectroscopy as a probe of temperature-induced delocalization of electrons in nanoscale semiconductors

SCHOLARONE™
Manuscripts

Hard X-ray photon-in photon-out spectroscopy as a probe of temperature-induced delocalization of electrons in nanoscale semiconductors

Ofer Hirsch[†], Kristina Kvashnina[‡][॥], Christoph Willa[†], Dorota Koziej[†*]

[†]Laboratory Multifunctional Materials, Department of Materials, ETH Zürich, Vladimir-Prelog-Weg 5, 8093 Zurich, Switzerland

[‡]The European Synchrotron Research Facility, CS40220, 38043 Grenoble Cedex 9, France

[॥]Institute of Resource Ecology, Helmholtz-Zentrum Dresden-Rossendorf, P.O. Box 510119, 01314 Dresden, Germany

ABSTRACT: Hard X-ray photon-in photon-out spectroscopy has so far mainly been applied to investigate fundamental physical phenomena in superconductors and chemical reactivity of bio-inorganic, photocatalytic and catalytic materials. Here, we show with the example of Pr_6O_{11} nanoparticles, an n-type semiconductor, how high-energy resolution fluorescence detected (HERFD) X-ray absorption near edge structure (XANES) can be used to track the changes of partially filled f-bands. We observe a reversible variation of the spectral features related to the tetravalent Pr ions upon heating and cooling, whereas structural and chemical transformations can be excluded. We assign these changes to the occupancy of the O $2p$-Pr $4f$-band and show that they directly relate to changes in the electrical conductance. Our results demonstrate how HERFD-XANES can be used to particularly study *in situ* the electronic properties of *f*-electrons in a semiconductor, and how this method can be further extended to other classes of semiconducting nanomaterials.

INTRODUCTION

Semiconducting nanoparticle are the hub of many emerging applications ranging from thermoelectrics[1] to a variety of photocatalytic[2] and electronic devices.[3-6] Different techniques allow characterizing the electrical conductivity of nanomaterials, but most of them impose very strict requirements for the sample preparation, for example, the geometry and the properties of the electrical contacts. For nanomaterials, we still grapple with the overarching picture of different length scales, from the macroscopic electrical properties to the electronic states participating in the charge transfer. Particularly, accounting for the density of state and related parameters like metal-oxygen hybridization, delocalized charge carriers in respect to the elemental composition, electronic and crystal structure of nanoparticle at ambient conditions is still very challenging.

Hard X-ray photon-in photon-out spectroscopy is element and structure-sensitive and has been shown to probe changes in the density of unoccupied states of rare-earth materials during chemical reactions.[7-10] The pre-edge region probes the *f*-states directly via $2p{\rightarrow}4f$ quadrupole transitions and a full RIXS map of this region

gives further insights into the exact nature of those states.[11] Whereas, in the HERFD-XANES spectrum, shape and position of edge and number, position and intensity of the features in the post-edge resolve the correlation between RE valence and *f*-electron occupancy.[8, 11]

Here we demonstrate that hard X-ray photon-in photon-out spectroscopy can be used as a contactless probe to track the temperature-induced changes of the delocalization of *f*-electrons, which are taking part in the electrical conductivity. To this end, we focus on Pr_6O_{11} because it is an n-type semiconductor exhibiting rich spectroscopic features related to *f*-electrons in the Pr L_3-edge HERFD-XANES and RIXS spectra. The conduction mechanism in Pr_6O_{11} is described with the small polaron model, where the dimensions of the polarons are of the same size as the distance between two sites in the lattice.[12] The *f*-states of Pr and the O $2p$-states overlap, hybridize and form a band.[13] The local coordination and hence the crystal structure determines the degree of hybridization and the filling level of this band. We calculate the RIXS maps of tri-, tetra- and mixed-valent Pr and correlate them with the measured HERFD-XANES spectra during temperature-induced

transformation of $Pr(OH)_3$ to Pr_6O_{11}. Surprisingly, we observe strong discrepancies between spectra of Pr_6O_{11} measured at room and at high temperatures, whereas the *in situ* PXRD and TGA remain unchanged. Thus, we can fully exclude the chemical and structural transformation. Upon repeated heating and cooling of the Pr_6O_{11} nanoparticles, we observe a reversible variation of the spectral features related to the tetravalent Pr ions. We can unambiguously assign these changes to the occupancy of the O $2p$-Pr $4f$-band and show that they directly relate to changes in the electrical conductance.

EXPERIMENTAL SECTION AND CALCULATIONAL METHODS

Nanoparticle synthesis. The synthesis of $Pr(OH)_3$ nanoparticles is analogous to the previously reported synthesis of $La(OH)_3$.[7] All chemicals were stored and handled in an oxygen- and water-free atmosphere in a glovebox and used as purchased without further purification. Acetophenone (4.68 ml, 40 mmol, 99.0% Fluka) was added to $Pr(O^iPr)$ (159.09 mg, 0.5 mmol, 99.9% Strem Chemicals) in a reaction vessel containing a stirring magnet. The vessel was sealed with a Teflon cap and the reaction was carried out in a CEM Discovery microwave reactor at 200 °C for 20 min. The synthesized particles were separated from the reaction liquid by centrifugation and washed twice with ethanol and once with acetone and dried at 60 °C 12 hours. To determine the temperature at which the phase transformation from $Pr(OH)_3$ to Pr_6O_{11} is fully completed, we measured *in situ* PXRD (Supplementary Information (SI) Fig. S1). Pr_6O_{11} nanoparticles, used here as a reference, were obtained by heating the $Pr(OH)_3$ powder to 500 °C for 2 h with a heating rate of 5°C/min.

X-ray spectroscopy. HERFD-XANES experiments were carried out at ID26 at the European Synchrotron Research Facility in Grenoble, France. The incident beam energy was set to the Pr L_3 edge at 5964 eV selected with a double Si (111) monochromator. The spectrometer in Rowland geometry was tuned to the maximum of Pr $L\beta_2$ emission line at 5849.63 eV with three spherically bent Ge (333) crystals at a Bragg angle of 77°. The total energy resolution was 0.85 eV. A typical HERFD-XANES scan was measured from 5945 to 6050 eV with a step size of 0.1 eV and took 300 s per scan. The RIXS maps were measured from 5954 to 5964 eV in the incident energy range and from 5840 to 5857 eV in the emission energy range with a step size of 0.1 eV and 0.4 eV, respectively. The *ex situ* measured reference samples were pressed into pellets of 2.5 mg of $Pr(OH)_3$ or Pr_6O_{11} nanoparticles and 20 mg BN. For the *in situ* heating experiments, a capillary was filled with $Pr(OH)_3$ and placed in a custom made furnace from the ESRF sample environmental pool and heated to 800 °C with a heating rate of 5 °C/min. HERFD-XANES was continuously recorded, 300 s per scan.

Valence-to-core (vtc) X-ray emission spectroscopy (XES) was measured on the same spectrometer equipped with four spherically bent Ge (333) crystals at a Bragg angle of 73°. The incident beam energy was fixed at 5976.5 eV and the emission was measured from 5890 to 5971.5 eV with a step size of 0.3 eV.

Multiplet Calculations. The multiplet calculations were performed with the MissingCode program[14-15] for $Pr3+$ and $Pr4+$ ions. First, the absorption process of the $2p{\rightarrow}4f$ quadrupole transitions was calculated, followed by the emission resulting from a $4d{\rightarrow}2p$ dipole transition. The considered electron configurations were $2p^6 4d^{10} 4f^N {\rightarrow} 2p^5 4d^{10} 4f^{N+1} {\rightarrow} 2p^6 4d^9 4f^{N+1}$. The intensities of the different final states were calculated with the Kramers-Heisenberg equation,[11, 16] including a core-hole lifetime broadening of the $2p$ of 3 eV and of the $4d$ hole of 0.5 eV with an instrumental broadening of 0.3 eV for the incident beam and 0.6 eV for the analyzer crystals. The calculations took $4f$-$4f$, $2p$-$4f$, and $4d$-$4f$ interactions as well as the spin-orbit coupling of the open shells into account. The values of the Slater integrals were taken from the Cowan code and were scaled to 80% for the different interactions. The spin-orbit coupling was not scaled. The values of the reduced Slater-integrals are listed in Table S1, SI.

Evaluation of RIXS maps and *in situ* data. The RIXS maps were calculated on the basis of multiplet theory. The multiplet calculations were performed with the MissingCode program[14-15] for Pr^{3+} and Pr^{4+} ions, where we calculated first the quadrupole absorption process, followed by the emitting dipole transition. The final state intensities were calculated with the Kramers-Heisenberg equation,[11, 16] including a core-hole lifetime broadening at the intermediate ($2p$ hole) and final ($4d$ hole) state and additional broadening due to the incident beam width and resolution of the analyzer crystals. The Slater-integral values for the different interactions were taken from the Cowan code and scaled to 80%. All reduced values are listed in Table S1, SI.

The *in situ* HERFD-XANES data were treated with the fityk program (Version 0.9.8).[17] All normalized spectra were first fitted with an arctangent step function and the spectral features were fitted with SplitGaussians. Four such functions were fitted into the Pr_6O_{11} HERFD-XANES spectra and the energy positions of the maxima were saved. Afterward, the *in situ* spectra were fitted with two, three, or four SplitGaussians (see text) with their maxima fixed to the *ex situ* determined values. The areas of the fitted Gaussians were used to determine the *f*-electron occupancy, n_f,[8, 18-19] with equation 1.

$$n_f = 1 + \frac{A(f^2) + A(f^2 \underline{L})}{A_{eg}(f^1) + A_{t2g}(f^1) + A(f^2) + A(f^2 \underline{L})},$$

(1)

where, $A(f_n)$, corresponds to the area of the fitted SplitGaussians of the respective feature.

The *in situ* pre-edge analyses were carried out with Matlab's trapz-function to obtain the area under the pre-edge up to an energy of 5960 eV (dashed line in Fig. 2c). We normalized the area by the area of the spectra measured at 25 °C,
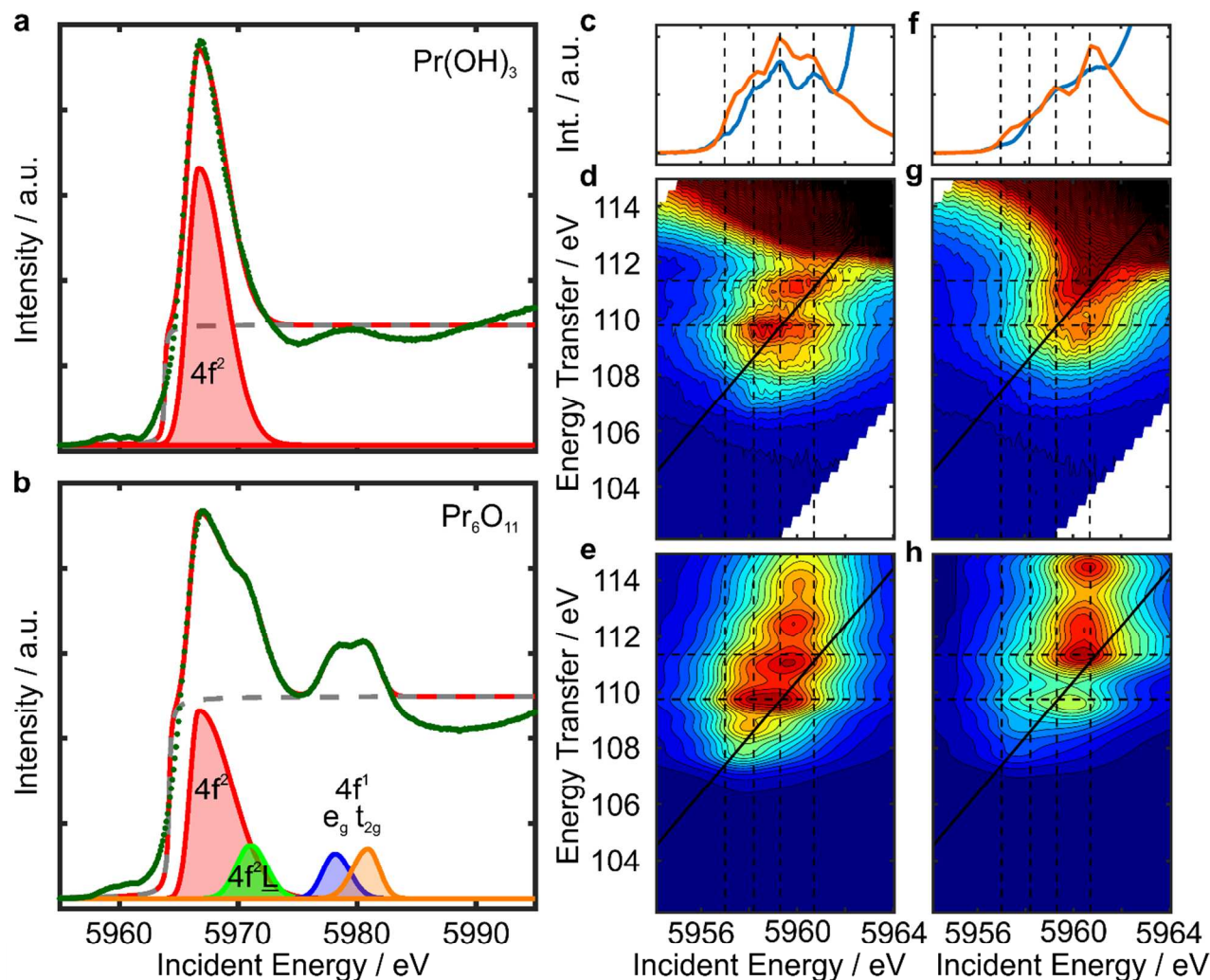
Figure 1. The experimental HERFD-XANES spectra (a-b) and experimental and calculated RIXS maps (c-h) of trivalent and mixed-valence praseodymium reference compounds. (a, b) De-convolution of the HERFD-XANES spectra of the $Pr(OH)_3$ and Pr_6O_{11} nanoparticles, respectively. The $4f^2$ (red), $4f^2\underline{L}$ (green), and the two $4f^1$ features split by the crystal field (blue, orange) are fitted with SplitGaussians. The edge jump, fitted with an arctangent function, is shown as gray dashed line. (c-e) The measured (d) and calculated (e) RIXS map for trivalent $Pr(OH)_3$ shows four distinct features. (f-h) The measured (g) and calculated (h) RIXS maps of the mixed valence oxide Pr_6O_{11}. The pre-edge RIXS was calculated as a linear combination of Pr^{3+} and Pr^{4+}. The dashed lines are guidelines for the eyes. The diagonal, bold, dashed line indicates the fixed emission energy of 5849.63 eV, and the corresponding pre-edge spectra at this energy are extracted from the calculated maps (orange curve) and compared with the measured pre-edge spectra of $Pr(OH)_3$ and Pr_6O_{11} (blue curve) in (c) and (f).

$$n_A = 1 - \frac{A}{A(25\,^\circ C)}$$

$$(2)$$

where A is the area below the pre-edge at a given temperature and $A(25\,^\circ C)$ the pre-edge area for the first *in situ* measurement of $Pr(OH)_3$ at 25 °C.

PXRD. *In situ* PXRD data was collected on a Panalytical Empyrean diffractometer equipped with a PIXCEL1D detector using Cu Kα radiation. The $Pr(OH)_3$ powder was prepared on an Al_2O_3 sample holder and mounted in an AP HTK-1200N oven. The incident beam optics consisted of 0.04 Soller slits, a divergence slit of 1/4°, and an anti-scatter slit of 1/2°. On the diffracted beam side, 0.04 Soller slits, a Ni-filter, and a 1/4° divergence slit were used.

Additionally, high-resolution synchrotron PXRD data were collected at the Swiss-Norwegian Beamline at the ESRF with a Dectris Pilatus2M detector and an incident energy of 17780.61 eV corresponding to a wavelength of 0.69730 Å. The nanoparticles were filled into a quartz capillary, which was mounted on a goniometer head and rotated. The acquisition time was 60 s per sample. Rietveld refinement was performed using the FullProfSuite software.[20-21] The background was defined as a linear interpolation of background points with refineable height and the peak shape function used to fit the patterns was the pseudo Voigt function with axial divergence asymmetry. The analysis of the Pr_6O_{11} pattern

recorded with high resolution further confirms the monoclinic Pr_6O_{11} phase (Fig. S1 and S2, SI).

TEM. Transmission electron microscopy measurements were conducted on a Philips Tecnai F30 operated at 300 kV in the Scientific Center for Optical and Electron Microscopy (ScopeM) of the ETH Zurich. A Gatan 1k CCD chip was used for image acquisition via the software Digital Micrograph (Fig. S3, SI).

XPS. X-ray photoelectron spectroscopy was recorded on a Sigma 2 spectrometer (Thermo Scientific) using a polychromatic Al Ka X-ray source and the binding energy was calibrated taking C 1s = 284.4 eV (Fig. S4, SI).

TGA. Thermogravimetric analysis (TGA) was measured with a Mettler Toledo TGA/SDTA851e instrument. 7.71 mg of $Pr(OH)_3$ powder were heated in an alumina crucible to 800 °C at a rate of 10 °C/min in air. After cooling down to 50 °C the powder was reheated to 350 °C at 10 °C/min as shown in Fig. S1b. SI.

Resistance Measurements. The Pr_6O_{11} film was prepared on an alumina substrate, which was equipped with interdigitated platinum electrodes for the resistance measurements on the top side and with a meander type platinum heating element on the back side. A dispersion of 200 mg of washed, but still wet, $Pr(OH)_3$ nanoparticles mixed with 5 ml of ethanol was prepared. The substrate was heated to 75 °C and 10 μl of the dispersion was drop caste ten times on the substrate. Finally, the substrate with the film was heated to 500 °C for two hours at a heating rate of 5 °C/min. Resistance was measured in a Teflon chamber under 200 ml/min flow of dry synthetic air. The resistance of the film was measured with a Keithley 617 programmable electrometer and the temperature was adjusted using a DC power supply.

RESULTS

The challenge in studying the mixed valence Pr_6O_{11} is to unequivocally assign the spectral features related to 3+ and 4+ valence of Pr. Thus, we study $Pr(OH)_3$ as a trivalent reference and compare its spectral features with Pr_6O_{11} as shown in Fig. 1. We perform the experiments at the Pr L_3 edge ($2p{\rightarrow}5d$) absorption line and record the Pr $L\beta_{2,5}$ emission line ($4d{\rightarrow}2p$). The spectrometer setup in HERFD-XANES reduces the core-hole lifetime broadening from 3.6 eV $(2p)$[22] to the 0.7 eV $(4d)$[23-25], which is in the range of the experimental resolution of 1 eV. In the $Pr(OH)_3$ spectrum, we assign the single feature to the $4f^2 5d^1$ state as shown in Fig. 1a. The $4f^3\underline{L}5d^{1,}$ state, where $\underline{L}$ denotes a hole in the ligand O $2p$ orbital, is not visible due to broadening of Pr $5d$ states related to oxygen as neighboring atoms.[26] In the spectrum of Pr_6O_{11}, additionally to the $4f^2 5d^1$ final state characteristic for Pr^{3+}, we observe three more features, which manifest the presence of Pr^{4+} as shown in Fig. 1b. The quasi-cubic like surrounding of the Pr ions in the monoclinic Pr_6O_{11} results in a cubic crystal field splitting of the states into an e_g and t_{2g} state with an energy difference of 2.8 eV.[27] Thus, by analogy to CeO_2 and PrO_2, we assign the features at
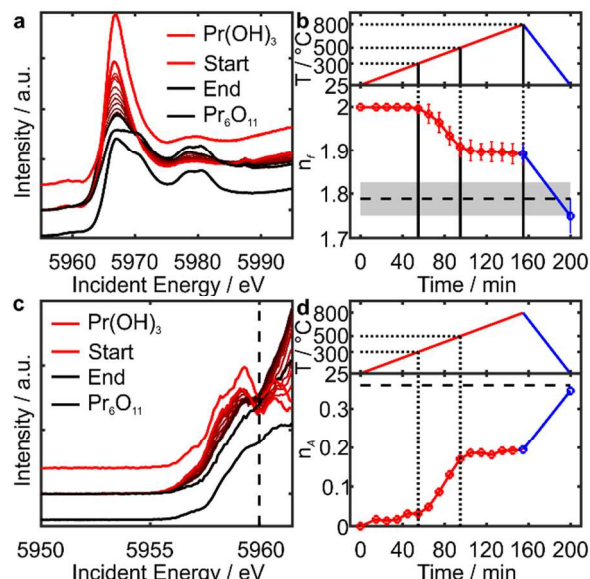
5978.2 eV (blue) and 5980.9 eV (orange) to the $4f^1 5d^1$ final state.[18-19, 28-29] The t_{2g} final state of $4f^2\underline{L}5d^1$

Figure 2. *In situ* HERFD-XANES studies of the temperature-induced phase transition from $Pr(OH)_3$ to Pr_6O_{11}. The reference spectra of $Pr(OH)_3$ and Pr_6O_{11} measured at RT are down-/up-shifted, respectively. (a, b) HERFD-XANES spectra measured at RT and then every 50 °C from 50 °C to 800 °C and the corresponding *f*-electron occupancy n_f as a function of time and temperature. As expected, the formation of Pr^{4+} ions at 300 °C leads to the decrease of the *f*-electron occupancy. Additionally, the n_f strongly decreases towards RT and reaches the *ex situ* determined value of 1.79± 0.04 (gray area). This demonstrates the changing occupancy of the O 2*p*-Pr 4*f* band with temperature. (c, d) Pre-edge spectra and the corresponding normalized pre-edge area, n_A, confirm the formation of Pr_6O_{11}. The increase of n_A together with the shape conservation of the pre-edge at RT after cooling down supports the higher delocalization at high temperatures rather than an oxidation of Pr^{3+} to Pr^{4+} upon cooling.

appears at 5971.0 eV,[18] whereas the e_g peak overlaps with $4f^2 5d^1$ of Pr^{3+}.

From a theoretical point of view, it is challenging to treat the partly filled 4*f* orbitals of the RE ions. In the sesquioxides RE_2O_3, the RE donates three electrons from the outer shells to the bond and the remaining 4*f* electrons stay strongly localized at the trivalent metal ion.[13] For Ce, Tb, and Pr also tetravalent ions exist and due to the hybridization with the O 2*p* states the *f*-electron occupancy takes a non-integer value, which results in a certain degree of delocalization. Here, Pr^{3+} represents a $4f^2$ configuration and Pr^{4+} a $4f^1$ and $4f^2\underline{L}$ configuration, which includes a delocalization of the 4*f* states. The relation between those

well-resolved features allows determining the *f*-electron occupancy (n_f) and the formal valence (*v*) with high accuracy. Here, the Pr^{4+}/Pr^{3+} ratio is 0.53 ± 0.13, valence $v = 3.53 \pm 0.13$,[30] which is close to the expected value of 3.66 for Pr_6O_{11}. The n_f of Pr_6O_{11} is 1.79 ± 0.04, which is as expected higher than 1.65 determined with conventional XANES for the stoichiometric PrO_2.[31]

Furthermore, in the pre-edge region we observe strong differences between $Pr(OH)_3$ and Pr_6O_{11}. We record the RIXS maps because the quadrupole transitions from $2p \rightarrow 4f$

Figure 3. Reversible changes of the *f*-electron occupancy in Pr_6O_{11} upon heating and their correlation with the electrical conductance. (a) The temperature-induced changes of resistance of Pr_6O_{11} films (b) The dependence of the conductance, $\ln(G_n/G_{RT})$, to the temperature during heating and cooling (left axis). The reversible changes of the conductance with temperature illustrate the effect of the electron delocalization on this macroscopic property. Both the analysis of the *f*-electron occupancy, n_f (top right axis), and the normalized pre-edge area, n_A (bottom right axis), show the higher occupancy of the O 2*p*-Pr 4*f* band at higher temperature. (c) A model of O 2*p*-Pr 4*f* hybridization is shown. The $4f^2\underline{L}$ feature increases with temperature resulting in higher *f*-electron occupancy. (top) The artistic view on the delocalized of electrons at different temperatures and (bottom) the corresponding HERFD-XANES spectra. The blue and red colors refer to the low and high temperature, respectively.

states are spread out differently in the incident beam and energy transfer directions depending on the number of localized *f*-electrons, shown in Fig. 1c-h.[11] In the RIXS map calculations, we do not take into account dipole $2p \rightarrow 5d$ transitions and mixing of the 5*d* states with the $4f^2$ states, but instead solely focus on the process $2p \rightarrow 4f$ and $4d \rightarrow 2p$. For $Pr(OH)_3$, the calculated RIXS maps reproduce very well all four features with the correct broadening in incident energy and energy transfer (Fig. 1c-e). In the Pr_6O_{11} RIXS maps, the four features distinguished in the $Pr(OH)_3$ sample are clearly visible, but have different relative intensities due to the presence of tetravalent Pr ions (Fig. 1f-h). We calculate the Pr_6O_{11} maps as a linear combination of Pr^{3+} (Fig. 1e) and Pr^{4+} (Fig. S5, SI) maps and take two trivalent and four tetravalent ions into account. The relative intensities of the features in the calculations and the measured intensities are in the right order of magnitude, while the calculation underestimates the broadening.

We study the emergence of Pr^{4+} by monitoring the *f*-electron occupancy (n_f) and the normalized area below the pre-edge (n_A) during the temperature-induced phase-transformation from $Pr(OH)_3$ to Pr_6O_{11}, as shown in Fig. 2 and Fig. S1, SI. At 300 °C, a decrease of n_f and an increase of n_A sets in and reaches a plateau above 500 °C. We assign these changes to the formation of Pr^{4+}, which is in line with the phase transformation from $Pr(OH)_3$ to Pr_6O_{11} observed in PXRD and TGA studies. Surprisingly, upon cooling from 800 °C to room temperature (RT) n_f and n_A further strongly change to finally reach the values measured for the reference compound at RT. The possible explanation for the sharp decrease of the n_f and increase of n_A upon cooling can be either a further oxidation of Pr^{3+} to Pr^{4+} or temperature-induced changes of the occupancy of the O 2*p*-Pr 4*f* band. As shown in Fig. S6, SI, the mass loss between 800 °C and 50 °C is only 0.5% and thus we can discard the hypothesis of oxidation of Pr^{3+} to Pr^{4+}. An inspection of the spectra measured at 800 °C and RT reveal that in both cases we observe all the post-edge features of Pr_6O_{11}, but at RT the white line maximum is flat. In the pre-edge, the two features at 5958.2 eV and
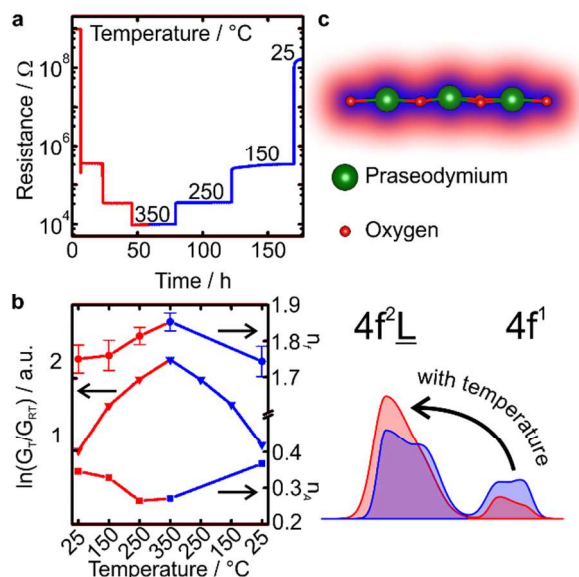
5959.3 eV are characteristic for the $4f^2$ state (Fig. 1c-e). For the measurements at 800 °C and RT, the relative intensities of those shoulders are very similar. However, at RT all the pre-edge features are generally shifted to higher energies. This finding supports the assumption of a higher delocalization at elevated temperatures rather than a shift from $4f^1$ to $4f^2$ or vice versa. The shift of the pre-edge to lower energies with a higher degree of f-state delocalization was observed for CeO_2 nanoparticles.[8] Furthermore, for the transition metals a temperature dependency of the quadrupole transitions due to the additional vibrational modes was reported.[32-33]

To further test our hypothesis we heat Pr_6O_{11} nano-powders again from RT to 350 °C and compare the spectroscopic changes (n_f, n_A) with the resistance measurements of the Pr_6O_{11} films ($\ln(G/G_{RT})$) as shown in Fig. 3a-b and Fig. S7a-b, SI. We determine the electronic band gap of the Pr_6O_{11} nanoparticles from valence-to-core X-ray emission spectroscopy (vtc XES) and HERFD-XANES to be 2.04 eV as shown in Fig. S8, SI. As expected for an n-type semiconductor, the resistance R_n of the Pr_6O_{11} film decreases by five orders of magnitude upon heating to 350 °C, and recovers to the almost initial value after cooling. This can be explained by the dependency of the delocalized charge carrier concentration on temperature, which is proportional to $\exp(-E/k_BT)$, where E is the energy needed to excite electrons into the conduction band. In this temperature range, we can exclude any phase transition (see Fig. S7 c-d, SI), but we still observe reversible changes of n_f and n_A upon cooling and heating. We compile all the information extracted from the HERFD-XANES studies and resistance measurements to visualize how the temperature-induced delocalization of f-electrons affects the spectral features as shown in Fig. 3c.

CONCLUSION

In summary, the electrical measurements are in line with the findings based on X-ray spectroscopy. Upon heating, we observe a higher degree of delocalization of the f-electrons and therefore a higher electrical conductivity.

The analysis of HERFD-XANES spectra and RIXS maps allows us to unambiguously distinguish between the temperature-induced changes of the Pr valence state from the changes exclusively related to delocalization of the f-electrons. Therefore, the photon-in photon-out method can be used as a contactless probe of the delocalized electrons in the conduction band of semiconductors.

As worldwide high brilliance sources and emission spectrometers are under rapid development, we anticipate that this work will trigger a further application of this method to monitor electrical properties of semiconducting nanomaterials in operando conditions and will be particularly interesting in the field of thermo-electrics.

ASSOCIATED CONTENT

The Supporting Information is available free of charge on the ACS Publications website. The electronic band gap determination, RIXS calculations for Pr^{4+}, TEM images, XPS data, *in situ* PXRD and TGA data, reheated HERFD-XANES, PXRD, and TGA data, and HR-PXRD of $Pr(OH)_3$ and Pr_6O_{11} are shown. The reduced Slater integrals for the multiplet calculations are listed.

AUTHOR INFORMATION

Corresponding Author

*E-Mail: dorota.koziej@mat.ethz.ch

Notes

The authors declare no competing financial interest.

ACKNOWLEDGMENT

REFERENCES

(1) Snyder, G. J., Toberer, E. S., Complex thermoelectric materials. *Nat. Mater.* **2008**, *7*, 105-114.

(2) Friebel, D., Louie, M. W., Bajdich, M., Sanwald, K. E., Cai, Y., Wise, A. M., Cheng, M.-J., Sokaras, D., Weng, T.-C., Alonso-Mori, R., Davis, R. C., Bargar, J. R., Nørskov, J. K., Nilsson, A., Bell, A. T., Identification of Highly Active Fe Sites in (Ni,Fe)OOH for Electrocatalytic Water Splitting. *J. Am. Chem. Soc.* **2015**, *137*, 1305-1313.

(3) Franklin, A. D., Nanomaterials in transistors: From high-performance to thin-film applications. *Science* **2015**, *349*, DOI: 10.1126/science.aab2750.

(4) Fiori, G., Bonaccorso, F., Iannaccone, G., Palacios, T., Neumaier, D., Seabaugh, A., Banerjee, S. K., Colombo, L., Electronics based on two-dimensional materials. *Nat. Nano.* **2014**, *9*, 768-779.

(5) Radisavljevic, B., Kis, A., Mobility engineering and a metal–insulator transition in monolayer MoS_2. *Nat. Mater.* **2013**, *12*, 815-820.

(6) Zheng, H., Rivest, J. B., Miller, T. A., Sadtler, B., Lindenberg, A., Toney, M. F., Wang, L.-W., Kisielowski, C., Alivisatos, A. P., Observation of transient structural-transformation dynamics in a Cu_2S danorod. *Science* **2011**, *333*, 206-209.

(7) Hirsch, O., Kvashnina, K. O., Luo, L., Süess, M. J., Glatzel, P., Koziej, D., High-energy resolution X-ray absorption and emission spectroscopy reveals insight into unique selectivity of La-based nanoparticles for CO_2. *Proc. Natl. Acad. Sci.* **2015**, *112*, 15803-15808.

(8) Cafun, J.-D., Kvashnina, K. O., Casals, E., Puntes, V. F., Glatzel, P., Absence of Ce^{3+} sites in chemically active colloidal ceria nanoparticles. *ACS Nano* **2013**, 7, 10726-10732.

(9) Safonova, O. V., Guda, A. A., Paun, C., Smolentsev, N., Abdala, P. M., Smolentsev, G., Nachtegaal, M., Szlachetko, J., Soldatov, M. A., Soldatov, A. V., van Bokhoven, J. A., Electronic and Geometric Structure of Ce^{3+} Forming Under Reducing Conditions in Shaped Ceria Nanoparticles Promoted by Platinum. *J. Phys. Chem. C* **2014**, *118*, 1974-1982.

(10) Koziej, D., Revealing Complexity of Nanoparticle Synthesis in Solution by in Situ Hard X-ray Spectroscopy—Today and Beyond. *Chem. Mater.* **2016**, *28*, 2478-2490.

(11) Kvashnina, K. O., Butorin, S. M., Glatzel, P., Direct study of the *f*-electron configuration in lanthanide systems. *J. Anal. At. Spectrom.* **2011**, *26*, 1265-1272.

(12) Rao, G. V. S., Ramdas, S., Mehrotra, P. N., Rao, C. N. R., Electrical transport in rare-earth oxides. *J. Solid State Chem.* **1970**, *2*, 377-384.

(13) Petit, L., Svane, A., Szotek, Z., Temmerman, W. M., First-principles study of rare-earth oxides. *Phys. Rev. B* **2005**, *72*, 205118.

(14) Butler, P. H., Point Group Symmetry and Applications - Methods and Tables. Plenum Press: New York, 1981.

(15) Cowan, R. D., *The Theory of Atomic Structure and Spectra*. University of California Press: Berkeley, California, 1981.

(16) Kotani, A., Shin, S., Resonant inelastic x-ray scattering spectra for electrons in solids. *Rev. Mod. Phys.* **2001**, *73*, 203-246.

(17) Wojdyr, M., Fityk: a general-purpose peak fitting program. *J. Appl. Crystallogr.* **2010**, *43*, 1126-1128.

(18) Bianconi, A., Kotani, A., Okada, K., Giorgi, R., Gargano, A., Marcelli, A., Miyahara, T., Many-body effects in praesodymium core-level spectroscopies of PrO_2. *Phys. Rev. B* **1988**, *38*, 3433-3437.

(19) Bianconi, A., Marcelli, A., Dexpert, H., Karnatak, R., Kotani, A., Jo, T., Petiau, J., Specific intermediate-valence state of insulating *4f* compounds detected by L_3 X-ray absorption. *Phys. Rev. B* **1987**, 35, 806-812.

(20) Young, R. A., *The Rietveld Method*. Oxford University Press: 1993.

(21) Rodríguez-Carvajal, J., Recent advances in magnetic structure determination by neutron powder diffraction. *Phys. B* **1993**, *192*, 55-69.

(22) Krause, M. O., Oliver, J. H., Natural widths of atomic K and L levels, Kα X-ray lines and several KLL Auger lines. *J. Phys. Chem. Ref. Data* **1979**, *8*, 329-338.

(23) Tanaka, S., Ogasawara, H., Okada, K., Kotani, A., Theory of the 4d→2p X-ray emission spectroscopy in Ce_2O_3, Pr_2O_3 and Dy_2O_3. *J. Phys. Soc. Jpn.* **1995**, *64*, 2225-2232.

(24) Ogasawara, H., Kotani, A., Thole, B. T., Lifetime effect on the multiplet structure of 4d x-ray-photoemission spectra in heavy rare-earth elements. *Phys. Rev. B* **1994**, *50*, 12332-12341.

(25) Ogasawara, H., Kotani, A., Potze, R., Sawatzky, G. A., Thole, B. T., Praseodymium 3d - and 4d-core photoemission spectra of Pr_2O_3. *Phys. Rev. B* **1991**, *44*, 5465-5469.

(26) Yamaoka, H., Sugiyama, H., Kubozono, Y., Kotani, A., Nouchi, R., Vlaicu, A. M., Oohashi, H., Tochio, T., Ito, Y., Yoshikawa, H., Charge transfer satellite in $Pr@C_{82}$ metallofullerene observed using resonant x-ray emission spectroscopy. *Phys. Rev. B* **2009**, *80*, 205403.

(27) Kotani, A., Kvashnina, K. O., Butorin, S. M., Glatzel, P., Spectator and participator processes in the resonant photon-in and photon-out spectra at the Ce L_3 edge of CeO_2. *Eur. Phys. J. B* **2012**, *85*, 1-13.

(28) Karnatak, R. C., Esteva, J. M., Dexpert, H., Gasgnier, M., Caro, P. E., Albert, L., X-ray absorption studies of CeO_2, PrO_2, and TbO_2. I. Manifestation of localized and extended *f* states in the 3d absorption spectra. *Phys. Rev. B* **1987**, *36*, 1745-1749.

(29) Dexpert, H., Karnatak, R. C., Esteva, J. M., Connerade, J. P., Gasgnier, M., Caro, P. E., Albert, L., X-ray absorption studies of CeO_2, PrO_2, and TbO_2. II. Rare-earth valence state by L_{III} absorption edges. *Phys. Rev. B* **1987**, *36*, 1750-1753.

(30) Yamaoka, H., Oohashi, H., Jarrige, I., Terashima, T., Zou, Y., Mizota, H., Sakakura, S., Tochio, T., Ito, Y., Sherman, E. Y., Kotani, A., X-ray spectroscopic study of the electronic structure of $Y_{1-x}Pr_xBa_2Cu_3O_7$. *Phys. Rev. B* **2008**, *77*, 045135.

(31) Tran, F., Schweifer, J., Blaha, P., Schwarz, K., Novák, P., PBE+*U* calculations of the Jahn-Teller effect in PrO_2. *Phys. Rev. B* **2008**, *77*, 085123.

(32) Durmeyer, O., Beaurepaire, E., Kappler, J. P., Ch., B., Baudelet, F., Temperature dependence of the pre-edge structure in the Ti K-edge X-ray absorption spectrum of rutile. *J. Phys.: Condens. Matter* **2010**, *22*, 125504.

(33) Brouder, C., Cabaret, D., Juhin, A., Sainctavit, P., Effect of atomic vibrations on the X-ray absorption spectra at the K edge of Al in a-Al_2O_3 and of Ti in TiO_2 rutile. *Phys. Rev. B* **2010**, *81*, 115125.